

Experimental realization of a quantum autoencoder via a universal two-qubit unitary gate

Chang-Jiang Huang,^{1,2} Qi Yin,^{1,2} Jun-Feng Tang,^{1,2} Daoyi Dong,³
Guo-Yong Xiang,^{1,2,*} Chuan-Feng Li,^{1,2} and Guang-Can Guo^{1,2}

¹Key Laboratory of Quantum Information, University of Science and Technology of China, CAS, Hefei 230026, China

²CAS Center For Excellence in Quantum Information and Quantum Physics

³School of Engineering and Information Technology,
University of New South Wales, Canberra, ACT 2600, Australia

(Dated: December 20, 2024)

ABSTRACT

As a ubiquitous aspect of modern information technology, data compression has a wide range of applications. Therefore, quantum autoencoder which can compress quantum information into a reduced space is fundamentally important to achieve automatical data compression in the field of quantum information. Such a quantum autoencoder can be implemented through training the parameters of a quantum device using machine learning. In this paper, we experimentally realize a universal two-qubit unitary gate and achieve a quantum autoencoder by applying machine learning. Also, this quantum autoencoder can be used to discriminate two groups of nonorthogonal states.

INTRODUCTION

The compression of information, one of the fundamental tasks in classical information theory, has been studied for many years [1–6]. With the development of Internet, massive data are generated and transferred within very short time. Thus, compressing data into the smallest possible space is of crucial importance in present-day digital technology. Various compression methods have found a wide range of applications such as text coding [3, 4], image compression [5, 6]. Correspondingly, in the quantum domain, the compression of quantum information has aroused widespread attentions [7, 8]. Many methods of compressing quantum data based on different specific assumptions on properties of the quantum states have been proposed and demonstrated [9–14]. Apart from exploiting a fixed structure of quantum data, devices called quantum autoencoders, which are capable of learning the structure based on a training data set, have been proposed and studied recently [15–17].

A traditional autoencoder can represent classical data in a lower-dimensional space. As illustrated in Fig.1(a), the information contained in input nodes is represented by fewer nodes after the initial encoder ε . If the compression is lossless, the decoder D can perfectly reconstruct the input bits at the output. Autoencoders form one of the core issues in many machine learning problems, and have many applications in image processing and other fields [18–20]. In recent years, quantum machine learning, which combines both quantum physics and machine learning, shows powerful capability in more and more applications [14, 21–27] and has become a booming research area attracting worldwide attention. Autoencoders for quantum data, which belong to the field of quantum machine learning, have aroused great interest in the field of quantum information recently [15–17]. For a quantum circuit to realize an autoencoder

network, as illustrated in Fig.1(b), a parameterized unitary $U^j(p_1, p_2, \dots, p_n)$ is trained as a quantum autoencoder where measurement results are considered and an optimization algorithm is employed.

In this paper, we experimentally realize a universal two-qubit unitary gate and achieve a quantum autoencoder based on a similar principle of the theoretical model in Ref. [16], but with some notable differences. Our quantum autoencoder can encode two 2-qubit pure states $|\varphi_1\rangle, |\varphi_2\rangle$ into two qubit states without any other restriction. Besides encoding qubits, our device can also be used to discriminate two groups of nonorthogonal states.

RESULTS

Quantum-classical hybrid scheme

Here we first introduce the quantum-classical hybrid scheme for quantum autoencoder proposed in Ref. [16]. As shown in Fig.1(b), the state preparation, operation and measurement are performed by quantum means while the optimization of parameters is realized via a classical algorithm. Fig.1(b) also indicates the scheme for our experiment: the core issue is to use the same 2-qubit unitary operator U to encode two 2-qubit states $|\varphi_1\rangle, |\varphi_2\rangle$ into two qubit states. In the classical scheme, we use a machine learning algorithm, stochastic gradient descent, to optimize the unitary transformation for compressing the quantum states. In a single iteration of our gradient descent algorithm, we perform the following steps:

1. Choose a random parameter p_k to optimize U^j . Set new parameters $p_1, \dots, p_k + a, \dots, p_n$ for U^j . Here a is a preset parameter indicating the extent of change at each step.
2. Prepare the input states $|\varphi_i\rangle$, and let it evolve under the encoding unitary U^j .

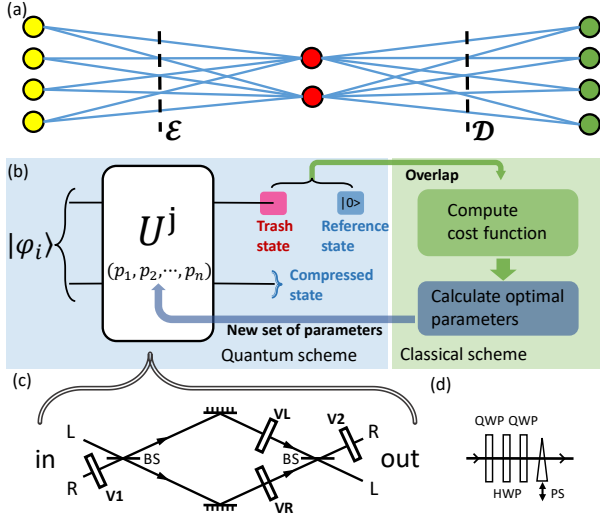


FIG. 1: (a) A graphical representation of encoding and decoding process. The map ϵ encodes the input data (yellow dots) into a lower-dimensional space (red dots). If the compression is lossless, the decoder D can perfectly reconstruct the input data at the output (green dots). (b) The hybrid scheme for training a quantum autoencoder in our experiment. The input state $|\varphi_i\rangle$ is compressed by parameterized unitary $U^j(p_1, p_2, \dots, p_n)$. When overlaps between trash state and reference state for all states in the input set are collected, a classical learning algorithm computes and sets a new group of parameters to the unitary $U^{j+1}(p_1, p_2, \dots, p_n)$. (c) Universal two-qubit unitary gate composed of two beam splitters, two mirrors and four same single-qubit parts (V1, V2, VR, VL). (d) Each single-qubit part is composed of two QWPs, a HWP, and a phase shifter (PS).

3. Measure and record the overlap between the trash state and the reference state.
4. Repeat steps 2-3 untill collecting the overlap of all states in $\{|\varphi_i\rangle\}$.
5. Record the average of the overlap in step 4 as x_+ .
6. Set new parameters $p_1, \dots, p_k - a, \dots, p_n$ for U^j and repeat steps 2-4. Then record the average of the overlap newly acquired in step 4 as x_- , and $1 - \frac{x_+ + x_-}{2}$ as the cost funtion in this iteration.
7. Renew the parameters using stochastic gradient descent algorithm. Specifically, we set the k th parameter p_k as $p_k + \frac{b}{a}(x_+ - x_-)$. Here b is another preset parameters indicating the extent of change at each iteration.

After some iterations of our algorithm, we renew the parameters a and b if the average cost funtion of continuous ten iterations is close to (or more than) the previous result. This strategy is used to reduce the stepsize and ensure the precision of our algorithm. All the above process is repeated until the cost funtion converges to 0.

Universal two-qubit unitary operator

Now, our task turns to realize a multi-qubit parameterized unitary operator. It is well known that any binary quantum alternative can serve as a qubit. Therefore, different degrees of freedom of one photon can represent several qubits. Thus, by choosing polarization and path degrees of freedom as two qubits, we can achieve the 2-qubit universal parameterized unitary gate combining path unitary gate with polarization gate [28].

The setup for a universal two-qubit unitary gate is shown in Fig.1(c). In a few words, for any given 2-qubit unitary operator:

$$U = \begin{bmatrix} U_{RR} & U_{RL} \\ U_{LR} & U_{LL} \end{bmatrix}$$

where U_{RR} (U_{RL}, U_{LR}, U_{LL}) is a 2×2 matrix referring to the path R/L alternative, they can be written as:

$$\begin{aligned} U_{RR} &= \frac{1}{2}V_2(V_R + V_L)V_1, \\ U_{LL} &= \frac{1}{2}(V_R + V_L), \\ U_{RL} &= -\frac{i}{2}V_2(V_R - V_L), \\ U_{LR} &= \frac{i}{2}(V_R - V_L)V_1. \end{aligned}$$

Here, V_1, V_2, V_R , and V_L are unitary polarization operators which can be easily realized by a set of half- and quarter-wave plates and phase shifters. Thus, universal 2-qubit unitary operator U can be achieved. See more details in supplementary materials.

Experimental setup

In the part of state preparation, since the *Mach – Zehnder* interferometer in Fig.1(c) is difficult to realize and keep phase stable, we use two phase stable Sagnac interferometers to separately implement state preparation and M-Z interferometer. At the beginning (Fig.2(a)), photon pairs with wave length $\lambda = 808$ nm are created by type-I spontaneous parametric down-conversion (SPDC) in a nonlinear crystal (BBO) which is pumped by a 40-mW beam at 404 nm. The two photons pass through two interference filters whose full width at half maximum is 3 nm. One photon is detected by a single-photon counting module (SPCM) as a trigger, another photon is prepared in the state of very pure horizontal polarization noted as $|H\rangle$ through a polarizer beam splitter (PBS). Then a half-wave plate (HWP) along with a PBS can control the path-bit of the photon. In each path, a HWP and a quarter-wave plate (QWP) are used to control the polarization of the photon, as shown in Fig.2(b). Thus, we can produce any expected phase stable two-qubit state thanks to the first Sagnac interferometer.

The parameterized unitary U is realized with the help of the second Sagnac interferometer in Fig.2(c). It is worth noting that there is a special beam-splitter cube which is half PBS-coated and half coated by non-polarizer beam splitter (NBS) in the

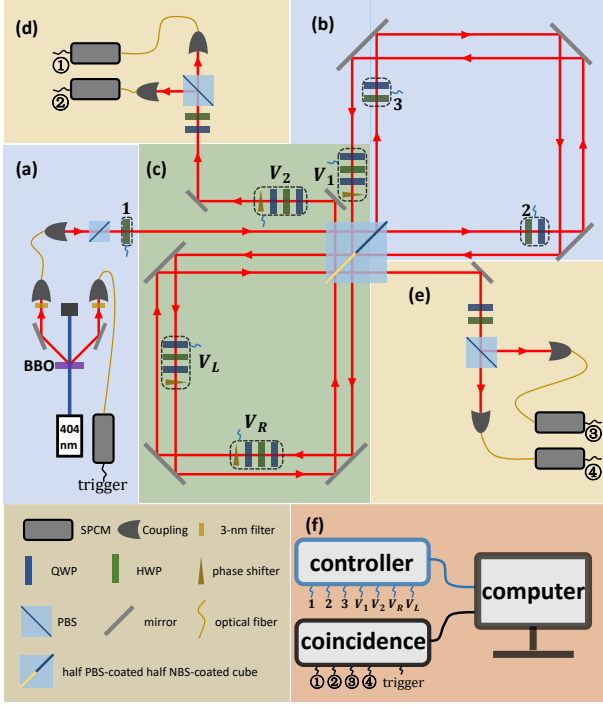


FIG. 2: Experiment setup for realizing a quantum autoencoder. The setup consists of three modules. (a)-(b) state preparation: Photon pairs are created by type-I SPDC through a BBO. One photon is set as a trigger and another photon is prepared in the state $|H\rangle$ through a PBS. Then a HWP along with a PBS can control the path-bit of the photon. In each path, a HWP and a QWP are used to control the polarization of the photon. (c)-(e) parameterized unitary U and measurements: The second Sagnac interferometer contains four unitary polarization operators V_1, V_2, V_R, V_L . Due to the structure of Sagnac interferometer, produced two-qubit states go through the NBS-coated surface twice. Thus, a parameterized universal two-qubit unitary gate is achieved. Then, a QWP, a HWP and a PBS can form any local measurements on polarization. (f) classical optimization algorithm: Our algorithm is mainly carried out by a computer and electronic-controlled devices.

junction of two Sagnac interferometers. The second Sagnac interferometer contains four unitary polarization operators V_1, V_2, V_R, V_L . Each of them is composed of two quarter-wave plates (QWP), a half-wave plate (HWP), and a phase shifter (PS), which are all electronic-controlled. Meanwhile, due to the structure of Sagnac interferometer, produced two-qubit states go through the NBS-coated surface twice. Thus, as illustrated before, we finally achieve the parameterized universal two-qubit unitary gate.

We can construct any local measurements on polarization just by a QWP, a HWP and a PBS in Fig.2(d)-(e). Our classical programme is mainly carried out by a computer and electronic-controlled devices including phase shifter, HWPs and QWPs.

Experimental results: tomography of two-qubit

unitary gate

Once we realize the universal two-qubit unitary gate, it is natural to ask how well our unitary gate performs. For characterization of our unitary gate, we estimate the process matrix using the maximum-likelihood method [29] for many different but significant gates such as identity gate, controlled-not gate, controlled-Z gate, controlled-Hadamard gate, SWAP gate, $\sqrt{i\text{SWAP}}$ gate and so on. Since the maximum-likelihood method needs joint measurement basis of path and polarization, we use a trick to reduce the difficulty of realizing joint measurements. We absorb the basis in the parameterized unitary U . For example, if we want to set path measurement basis as U^\dagger , we actually set our U as $U^\dagger \times U$. Some results of the process tomography are shown in Fig.3. Here we show the process matrix $\tilde{\chi}$ of controlled-not gate (polarization control path) and SWAP gate with the fidelity being 0.957 and 0.948, respectively. The real elements and the imaginary elements are plotted respectively, with ideal theoretical values overlaid. For clarity, we use red to represent positive and blue to represent negative. Full statistics are available in supplementary materials. Our fidelity is computed by $\text{tr} \sqrt{\sqrt{\chi_{exp}} \chi \sqrt{\chi_{exp}}}$. Here χ_{exp} is the experimental process matrix and χ is the theoretical process matrix. The average fidelity of our gates is 0.953.

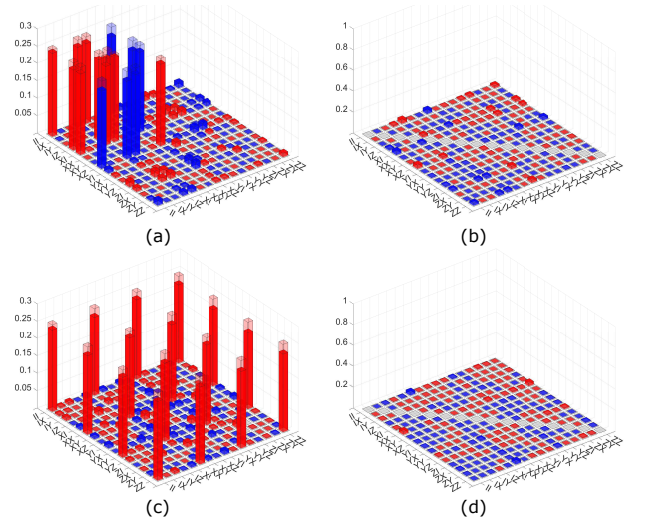


FIG. 3: Characterization of experimentally realized gates. A two-qubit gate can be described by its process matrix $\tilde{\chi}$. Specifically, each input state ρ is mapped to an output $\Sigma_{mn} \tilde{\chi}_{mn} \hat{E}_m \rho \hat{E}_n^\dagger$, where the summation is over all possible two-qubit Pauli operators \hat{E}_k . Here we plot the real elements in Fig.3(a) (Fig.3(c)) and the imaginary elements in Fig.3(b) (Fig.3(d)) of CNOT (SWAP), with ideal theoretical values overlaid. For clarity, we use red to represent positive and blue to represent negative. The fidelity of CNOT/SWAP is 0.957/0.948.

Experimental results: encoding quantum information into lower dimension

Now we turn to the core issue of encoding the quantum information into lower dimension. Our goal is to achieve a 2-qubit unitary operator U which can encode two 2-qubit states $|\varphi_1\rangle, |\varphi_2\rangle$ into two qubit states $|\varphi'_1\rangle, |\varphi'_2\rangle$. For example, we encode two 2-qubit states $|RH\rangle, |LV\rangle$ into states $|\varphi'_1\rangle|R\rangle, |\varphi'_2\rangle|R\rangle$. Here $|R\rangle/|L\rangle$ stands for path qubit and $|H\rangle/|V\rangle$ stands for polarization qubit. Thus, we can trash the path qubit and obtain the compressed states $|\varphi'_1\rangle, |\varphi'_2\rangle$ which maintain the original quantum information totally in polarization qubit. Similarly, encoding the information into path qubit is also feasible. Using the algorithm mentioned before, we can train our parameterized unitary operator U efficiently to accomplish the goal. Fig.4(a) (Fig.4(b)) shows the result of encoding $\{|RH\rangle, |LV\rangle\}$ into path (polarization) qubit. Here infidelity is the cost function in our algorithm and iterations indicate the train process. Results of encoding another set of states $\{\frac{1}{2}|RD\rangle + \frac{\sqrt{3}}{2}|LV\rangle, |LV\rangle\}$ into path (polarization) qubit is shown in Fig.4(c) (Fig.4(d)). The performance of our quantum autoencoder is related to the experimental conditions such as imperfect NBS-coated surface, unbalanced coupling efficiency, and uneven wave plates. Though under these imperfect conditions, the cost function can still approach 0 after a few iterations. See more data in supplementary materials.

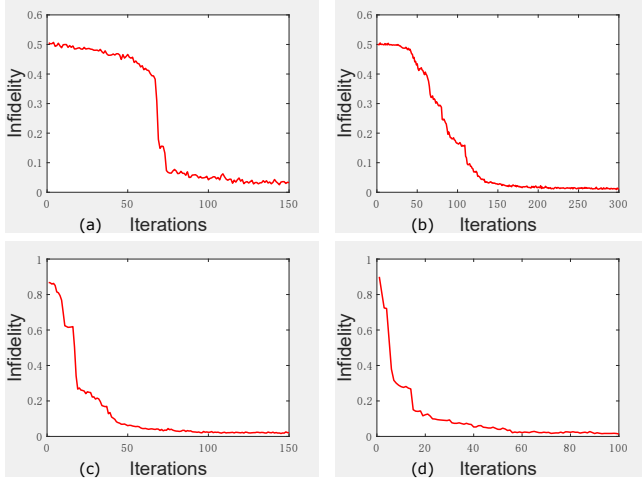


FIG. 4: The results of encoding two 2-qubit states into two qubit states. Here we show the results of encoding different initial states into different qubits (path/polarization). (a) encode $\{|RH\rangle, |LV\rangle\}$ into path qubit. (b) encode $\{|RH\rangle, |LV\rangle\}$ into polarization qubit. (c) encode $\{\frac{1}{2}|RD\rangle + \frac{\sqrt{3}}{2}|LV\rangle, |LV\rangle\}$ into path qubit. (d) encode $\{\frac{1}{2}|RD\rangle + \frac{\sqrt{3}}{2}|LV\rangle, |LV\rangle\}$ into polarization qubit. Here infidelity is the cost function in our algorithm and iterations indicate the train process.

Experimental results: discrimination between two different groups of nonorthogonal states

Apart from encoding quantum information into lower dimension, we find our quantum autoencoder can also realize the discrimination between two different groups of nonorthogonal states. Discrimination between nonorthogonal states has been an important task in quantum information [30–32]. Many methods have been proposed to solve this problem under different conditions. The most well-known ones are min-error discrimination [31, 33] and unambiguous discrimination [34–37]. It is natural to ask whether we may discriminate groups of nonorthogonal states. Some excellent works have been done [38, 39]. In our experiment, we find that we just need to encode different groups into orthogonal path/polarization qubits. For example, encode two groups of nonorthogonal states $\{|\phi_i\rangle\}, \{|\varphi_j\rangle\}$ into states $\{|\varphi'_i\rangle|R\rangle\}, \{|\varphi'_j\rangle|L\rangle\}$. Thus we can realize the bound of min-error discrimination between two different groups of nonorthogonal states after some iterations.

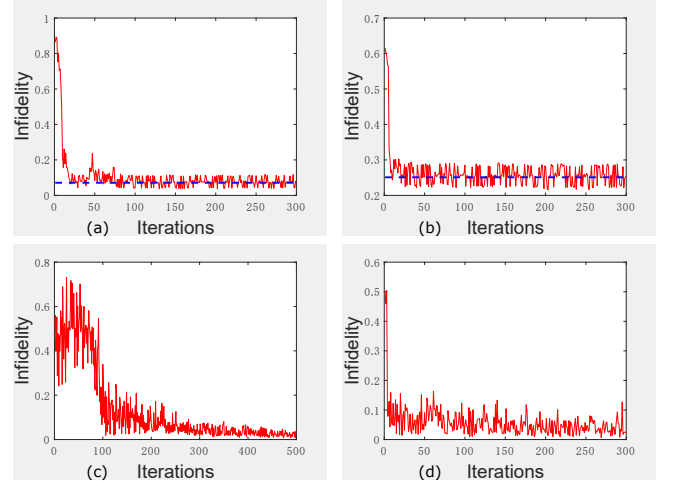


FIG. 5: The results of discriminating two different groups of nonorthogonal states. The bound for (a)-(b) is plotted in blue dashed line. (a) encode $\{\cos\theta_{1/2}|RH\rangle + \sin\theta_{1/2}|RV\rangle, \theta_{1/2} = \pm 4^\circ\}$ & $\{\cos\theta_{3/4}|RH\rangle + \sin\theta_{3/4}|RV\rangle, \theta_{3/4} = 60^\circ \pm 4^\circ\}$ into different polarization qubits. (b) encode $\{\cos\theta_{1/2}|RH\rangle + \sin\theta_{1/2}|RV\rangle, \theta_{1/2} = \pm 2^\circ\}$ & $\{\cos\theta_{3/4}|RH\rangle + \sin\theta_{3/4}|RV\rangle, \theta_{3/4} = 30^\circ \pm 2^\circ\}$ into different polarization qubits. (c) encode $\{\cos\theta_1|RH\rangle + \sin\theta_1|LH\rangle, \theta_1 \in [-50^\circ, 50^\circ]\}$ & $\{\cos\theta_2|RV\rangle + \sin\theta_2|LV\rangle, \theta_2 \in [-50^\circ, 50^\circ]\}$ into different path qubits, (d) encode $\{\cos\theta_1|RH\rangle + \sin\theta_1|RV\rangle, \theta_1 \in [-20^\circ, 20^\circ]\}$ & $\{\cos\theta_2|LH\rangle + \sin\theta_2|LV\rangle, \theta_2 \in [-20^\circ, 20^\circ]\}$ into different polarization qubits. Here infidelity is the cost function in our algorithm and iterations indicate the train process.

We follow the core principle in Ref. [31] to derive the error bound and the optimal strategies to realize the min-error discrimination between two groups. Similar to the case of compressing information, we can train our parameterized unitary operator U efficiently to accomplish the goal and reach the bound of min-

error discrimination between two different groups of nonorthogonal states. Some of the results are shown in Fig.5. The blue dashed line is the bound of min-error discrimination between two different groups of nonorthogonal states. We also show our agent's learning ability by encoding groups of path/polarization orthogonal states into orthogonal polarization/path states in Fig.5(c)-(d). Full data are available in supplementary materials.

DISCUSSION

In summary, we have experimentally demonstrated a simple but important scheme for a quantum autoencoder. We have shown that our device is able to compress two 2-qubits into two qubits without knowing the structure of the data set. We can also use the autoencoder to discriminate different groups of quantum states. Combining classical machine learning algorithm with quantum devices, quantum autoencoders have the valuable capability of adjusting different data sets and can process quantum information very well.

Comparing our scheme with the proposal of Ref. [16], we use a different cost function defined in terms of the occupation probability of the junk qubit, which requires a simple measurement of the qubit, rather than in terms of the overlap between a fixed reference state and part of the output of the encoding unitary operator, which is estimated via a SWAP test. During the writing of this article, we became aware of another, parallel experimental implementation of a quantum autoencoder, reported in Ref. [40]. Different from Ref. [40], our quantum autoencoder can compress two 2-qubits into two qubits. Our device can also realize the discrimination between two groups of nonorthogonal 2-qubit states and reach the theoretical bound.

Furthermore, although our experiment was designed for 2-qubits, the same design can be extended to compress higher-dimensional qubits or qunits [15–17, 40]. In that case, the number of input qubits and the size of the unitary operator would be increased.

SUPPLEMENTARY MATERIALS

Section S1. Universal two-qubit unitary gate

Section S2. Bound of min-error discrimination

Section S3. All experimental data

Fig. S1. The setup for universal two-qubit unitary gate

Fig. S2. - Fig. S8. Process matrices of different two-qubit unitary gates

Fig. S9. Results of encoding different initial states into path qubit

Fig. S10. Results of encoding different initial states into polarization qubit

Fig. S11. - Fig. S12. Results of discriminating different initial groups of states

Reference [28,31]

-
- * Electronic address: gyxiang@ustc.edu.cn
- [1] C. E. Shannon. A mathematical theory of communication. *Bell System Technical Journal* **27**, 379–423 (1948).
 - [2] J. Ziv, A. Lempel. A universal algorithm for sequential data compression. *IEEE Transactions on Information Theory* **23**, 337–343 (1977).
 - [3] D. A. Huffman. A method for the construction of minimum-redundancy codes. *Proceedings of the IRE* **40**, 1098–1101 (1952).
 - [4] I. H. Witten, R. M. Neal, J. G. Cleary. Arithmetic coding for data compression. *Communications of the ACM* **30**, 520–540 (1987).
 - [5] A. K. Jain. Image data compression: A review. *Proceedings of the IEEE* **69**, 349–389 (1981).
 - [6] W. B. Pennebaker, J. L. Mitchell. *JPEG: Still image data compression standard* (Springer Science & Business Media, 1992).
 - [7] R. Jozsa, B. Schumacher. A new proof of the quantum noiseless coding theorem. *Journal of Modern Optics* **41**, 2343–2349 (1994).
 - [8] R. Jozsa, M. Horodecki, P. Horodecki, R. Horodecki. Universal quantum information compression. *Physical Review Letters* **81**, 1714 (1998).
 - [9] C. H. Bennett, A. W. Harrow, S. Lloyd. Universal quantum data compression via nondestructive tomography. *Physical Review A* **73**, 032336 (2006).
 - [10] M. Plesch, V. Bužek. Efficient compression of quantum information. *Physical Review A* **81**, 032317 (2010).
 - [11] L. A. Rozema, D. H. Mahler, A. Hayat, P. S. Turner, A. M. Steinberg. Quantum data compression of a qubit ensemble. *Physical Review Letters* **113**, 160504 (2014).
 - [12] Y. Yang, G. Chiribella, D. Ebler. Efficient quantum compression for ensembles of identically prepared mixed states. *Physical Review Letters* **116**, 080501 (2016).
 - [13] Y. Yang, G. Chiribella, M. Hayashi. Optimal compression for identically prepared qubit states. *Physical Review Letters* **117**, 090502 (2016).
 - [14] S. Lloyd, M. Mohseni, P. Rebentrost. Quantum principal component analysis. *Nature Physics* **10**, 631 (2014).
 - [15] Y. Ding, L. Lamata, M. Sanz, X. Chen, E. Solano. Experimental implementation of a quantum autoencoder via quantum adders. *arXiv preprint arXiv:1807.10643* (2018).
 - [16] J. Romero, J. P. Olson, A. Aspuru-Guzik. Quantum autoencoders for efficient compression of quantum data. *Quantum Science and Technology* **2**, 045001 (2017).
 - [17] L. Lamata, U. Alvarez-Rodriguez, J. D. Martín-Guerrero, M. Sanz, E. Solano. Quantum autoencoders via quantum adders with genetic algorithms. *Quantum Science and Technology* **4**, 014007 (2018).
 - [18] Y. Guo, Y. Liu, A. Oerlemans, S. Lao, S. Wu, M. S. Lew. Deep learning for visual understanding: A review. *Neurocomputing* **187**, 27–48 (2016).
 - [19] W. Liu, Z. Wang, X. Liu, N. Zeng, Y. Liu, F. E. Alsaadi. A survey of deep neural network architectures and their applications. *Neurocomputing* **234**, 11–26 (2017).
 - [20] I. Goodfellow, Y. Bengio, A. Courville, Y. Bengio. *Deep*

- learning, vol. 1 (MIT Press, Cambridge, 2016).
- [21] G. D. Paparo, V. Dunjko, A. Makmal, M. A. Martin-Delgado, H. J. Briegel. Quantum speedup for active learning agents. *Physical Review X* **4**, 031002 (2014).
 - [22] A. Radovic, M. Williams, D. Rousseau, M. Kagan, D. Bonacorsi, A. Himmel, A. Aurisano, K. Terao, T. Wongjirad. Machine learning at the energy and intensity frontiers of particle physics. *Nature* **560**, 41 (2018).
 - [23] D. Dong, C. Chen, H. Li, T.-J. Tarn. Quantum reinforcement learning. *IEEE Transactions on Systems, Man, and Cybernetics, Part B (Cybernetics)* **38**, 1207–1220 (2008).
 - [24] J. Biamonte, P. Wittek, N. Pancotti, P. Rebentrost, N. Wiebe, S. Lloyd. Quantum machine learning. *Nature* **549**, 195 (2017).
 - [25] J. Carrasquilla, R. G. Melko. Machine learning phases of matter. *Nature Physics* **13**, 431 (2017).
 - [26] J. Wang, S. Paesani, R. Santagati, S. Knauer, A. A. Gentile, N. Wiebe, M. Petruzzella, J. L. O’Brien, J. G. Rarity, A. Laing *et al.* Experimental quantum hamiltonian learning. *Nature Physics* **13**, 551 (2017).
 - [27] Y. Shen, N. C. Harris, S. Skirlo, M. Prabhu, T. Baehr-Jones, M. Hochberg, X. Sun, S. Zhao, H. Larochelle, D. Englund *et al.* Deep learning with coherent nanophotonic circuits. *Nature Photonics* **11**, 441 (2017).
 - [28] B.-G. Englert, C. Kurtsiefer, H. Weinfurter. Universal unitary gate for single-photon two-qubit states. *Physical Review A* **63**, 032303 (2001).
 - [29] M. Ježek, J. Fiurášek, Z. Hradil. Quantum inference of states and processes. *Physical Review A* **68**, 012305 (2003).
 - [30] A. S. Holevo. Statistical decision theory for quantum systems. *Journal of Multivariate Analysis* **3**, 337–394 (1973).
 - [31] C. W. Helstrom. Quantum detection and estimation theory. *Journal of Statistical Physics* **1**, 231–252 (1969).
 - [32] A. Chefles. Quantum state discrimination. *Contemporary Physics* **41**, 401–424 (2000).
 - [33] S. M. Barnett, E. Riis. Experimental demonstration of polarization discrimination at the helstrom bound. *Journal of Modern Optics* **44**, 1061–1064 (1997).
 - [34] I. D. Ivanovic. How to differentiate between non-orthogonal states. *Physics Letters A* **123**, 257–259 (1987).
 - [35] D. Dieks. Overlap and distinguishability of quantum states. *Physics Letters A* **126**, 303–306 (1988).
 - [36] B. Huttner, A. Muller, J.-D. Gautier, H. Zbinden, N. Gisin. Unambiguous quantum measurement of nonorthogonal states. *Physical Review A* **54**, 3783 (1996).
 - [37] M. Mohseni, A. M. Steinberg, J. A. Bergou. Optical realization of optimal unambiguous discrimination for pure and mixed quantum states. *Physical Review Letters* **93**, 200403 (2004).
 - [38] M. Mohseni, A. M. Steinberg, J. A. Bergou. Optical realization of optimal unambiguous discrimination for pure and mixed quantum states. *Physical Review Letters* **93**, 200403 (2004).
 - [39] H. Chen, L. Wossnig, S. Severini, H. Neven, M. Mohseni. Universal discriminative quantum neural networks. *arXiv preprint arXiv:1805.08654* (2018).
 - [40] A. Pepper, N. Tischler, G. J. Pryde. Experimental realization of a quantum autoencoder: The compression of qutrits via machine learning. *Physical Review Letters* **122**, 060501 (2019).

Acknowledgements

Funding: The work at USTC is supported by the National Natural Science Foundation of China under Grants (Nos. 11574291, 11774334, 61828303, and 11774335), the National Key Research and Development Program of China (No.2017YFA0304100, No.2018YFA0306400), Key Research Program of Frontier Sciences, CAS (No.QYZDY-SSW-SLH003), Anhui Initiative in Quantum Information Technologies. D.D. also acknowledges the support of the Australian Research Council by DP190101566. **Author contributions:** G.-Y.X. conceived and supervised the project. C.-J.H. designed and implemented the experiments with the assistance from Q.Y., J.-F.T. and G.-Y.X. C.-J.H. analyzed the experimental data with the help of D.D., G.-Y.X., C.-F.L., and G.-C.G. C.-J.H., D.D., and G.-Y.X. wrote the paper with contributions from all authors. **Competing interests:** The authors declare no competing interests. **Data and materials availability:** All data needed to evaluate the conclusions in the paper are present in the paper or the Supplementary Materials. Additional data related to this paper may be requested from the authors.

Supplementary Materials for Experimental realization of a quantum autoencoder via a universal two-qubit unitary gate

S1. UNIVERSAL TWO-QUBIT UNITARY GATE

The setup for a universal two-qubit unitary gate [28] which combines path unitary gate with polarization gate is shown in Fig.S1.

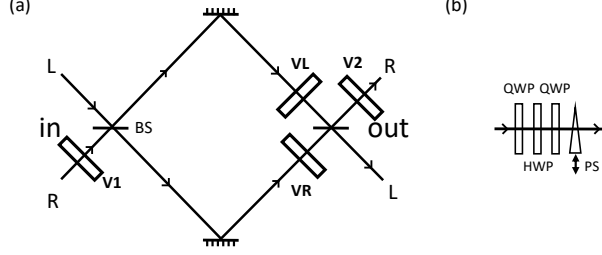


FIG. S1: (a) Universal two-qubit unitary gate which is composed of two beam splitters, two mirrors and four same single-qubit parts (V1,V2,VR,VL). (b) Each part is composed of two quarter-wave plates (QWP), a half-wave plate (HWP), and a phase shifter (PS).

The unitary operation of a symmetric beam splitter is given by:

$$U_{BS} = \frac{1}{\sqrt{2}}(|R\rangle\langle R| + |L\rangle\langle L| + i|L\rangle\langle R| + i|R\rangle\langle L|).$$

Here $|R\rangle/|L\rangle$ is path qubit which means the motional alternative of traveling to the right or to the left. Likewise, the joint operation of the mirrors inside the Mach-Zehnder setup is accounted for by the unitary operator:

$$U_{mirror} = -i(|L\rangle\langle R| + |R\rangle\langle L|),$$

where the inclusion of a phase factor $-i$ is a convenient convention because it gives $U_{BS}U_{mirror}U_{BS} = I$.

On one hand, the unitary gate U in Fig.S1(a) can be expressed as follows:

$$U = \begin{bmatrix} V_2 & 0 \\ 0 & I \end{bmatrix} U_{BS} \begin{bmatrix} V_R & 0 \\ 0 & V_L \end{bmatrix} U_{mirror} U_{BS} \begin{bmatrix} V_1 & 0 \\ 0 & I \end{bmatrix} \\ = \frac{1}{2} \begin{bmatrix} V_2 & 0 \\ 0 & I \end{bmatrix} \begin{bmatrix} I & i \\ i & I \end{bmatrix} \begin{bmatrix} V_R & 0 \\ 0 & V_L \end{bmatrix} \begin{bmatrix} 0 & -i \\ -i & 0 \end{bmatrix} \begin{bmatrix} I & i \\ i & I \end{bmatrix} \begin{bmatrix} V_1 & 0 \\ 0 & I \end{bmatrix}.$$

Here, I means 2×2 identity matrix for polarization qubit and $0/i$ means $0/i * I$. On the other hand, the unitary gate U can also be written as:

$$U = \begin{bmatrix} U_{RR} & U_{RL} \\ U_{LR} & U_{LL} \end{bmatrix}$$

where U_{RR} (U_{RL}, U_{LR}, U_{LL}) is a 2×2 matrix referring to the path R/L alternative. Since the two expressions above are actually the same form of the unitary gate U , the entries of this matrix can be written as:

$$U_{RR} = \frac{1}{2}V_2(V_R + V_L)V_1, \\ U_{LL} = \frac{1}{2}(V_R + V_L), \\ U_{RL} = -\frac{i}{2}V_2(V_R - V_L), \\ U_{LR} = \frac{i}{2}(V_R - V_L)V_1.$$

Thus, for any given 2-qubit unitary operator U , one can find four unitary polarization operators V_1, V_2, V_R, V_L , which can be easily realized by a set of half- and quarter-wave plates and phase shifters, such that the universal 2-qubit unitary operator U can be achieved.

S2. BOUND OF MIN-ERROR DISCRIMINATION

We follow the core principle in Ref. [31] to derive the error bound and the optimal strategies to realize the min-error discrimination between two groups. For simplicity, we consider two groups of the quantum states. Group a contains $\{|\Psi_{a1}\rangle, |\Psi_{a2}\rangle\}$ and group b contains $\{|\Psi_{b1}\rangle, |\Psi_{b2}\rangle\}$. Our goal is to figure out the strategy to minimize the probability of making an error in identifying the group with the probabilities $\{P_{a1}, P_{a2}, P_{b1}, P_{b2}\}$ for $\{|\Psi_{a1}\rangle, |\Psi_{a2}\rangle, |\Psi_{b1}\rangle, |\Psi_{b2}\rangle\}$. Here $P_{a1} + P_{a2} + P_{b1} + P_{b2} = 1$ and $\{|\Psi_{a1}\rangle, |\Psi_{a2}\rangle, |\Psi_{b1}\rangle, |\Psi_{b2}\rangle\}$ belong to a Hilbert space of $d=2$. We take the measurements as $\{\Pi_a, \Pi_b\}$ and outcome a/b (associated with the probability operator Π_a/Π_b) is taken to indicate that the state belongs to group a/b. The probability of making an error in classifying the state is given by:

$$\begin{aligned} P_{error} &= P_{a1}P(b|\Psi_{a1}) + P_{a2}P(b|\Psi_{a2}) + P_{b1}P(a|\Psi_{b1}) + P_{b2}P(a|\Psi_{b2}) \\ &= P_{a1}\langle\Psi_{a1}|\Pi_b|\Psi_{a1}\rangle + P_{a2}\langle\Psi_{a2}|\Pi_b|\Psi_{a2}\rangle + P_{b1}\langle\Psi_{b1}|\Pi_a|\Psi_{b1}\rangle + P_{b2}\langle\Psi_{b2}|\Pi_a|\Psi_{b2}\rangle \\ &= P_{a1} + P_{a2} - P_{a1}\langle\Psi_{a1}|\Pi_a|\Psi_{a1}\rangle - P_{a2}\langle\Psi_{a2}|\Pi_a|\Psi_{a2}\rangle + P_{b1}\langle\Psi_{b1}|\Pi_a|\Psi_{b1}\rangle + P_{b2}\langle\Psi_{b2}|\Pi_a|\Psi_{b2}\rangle \\ &= P_{a1} + P_{a2} - \text{tr}\{(P_{a1}|\Psi_{a1}\rangle\langle\Psi_{a1}| + P_{a2}|\Psi_{a2}\rangle\langle\Psi_{a2}| - P_{b1}|\Psi_{b1}\rangle\langle\Psi_{b1}| - P_{b2}|\Psi_{b2}\rangle\langle\Psi_{b2}|\Pi_a\}. \end{aligned}$$

This expression has its minimum value when the term $\text{tr}\{\dots\}$ reaches a maximum, which in turn is achieved if Π_a is a projector onto the positive eigenket of the operator $P_{a1}|\Psi_{a1}\rangle\langle\Psi_{a1}| + P_{a2}|\Psi_{a2}\rangle\langle\Psi_{a2}| - P_{b1}|\Psi_{b1}\rangle\langle\Psi_{b1}| - P_{b2}|\Psi_{b2}\rangle\langle\Psi_{b2}|$. We can obtain the solution using numerical calculation. For a specific solution, we limit the form of the states $\{|\Psi_{a1}\rangle, |\Psi_{a2}\rangle, |\Psi_{b1}\rangle, |\Psi_{b2}\rangle\}$ as follows: Without loss of generality we can choose the basis as $\{|0\rangle, |1\rangle\}$ such that the components of each state in this basis are real. Thus we can express the states $\{|\Psi_{a1}\rangle, |\Psi_{a2}\rangle, |\Psi_{b1}\rangle, |\Psi_{b2}\rangle\}$ as follows:

$$\begin{cases} |\Psi_{a1}\rangle = \cos\theta_1|0\rangle + \sin\theta_1|1\rangle \\ |\Psi_{a2}\rangle = \cos\theta_2|0\rangle + \sin\theta_2|1\rangle \\ |\Psi_{b1}\rangle = \cos\theta_1|0\rangle - \sin\theta_1|1\rangle \\ |\Psi_{b2}\rangle = \cos\theta_2|0\rangle - \sin\theta_2|1\rangle. \end{cases}$$

Here we assume $\theta_1 > \theta_2$ and $\{|0\rangle, |1\rangle\}$ are orthogonal bases of the Hilbert space. Hence, we can obtain the matrix expression of $P_{a1}|\Psi_{a1}\rangle\langle\Psi_{a1}| + P_{a2}|\Psi_{a2}\rangle\langle\Psi_{a2}| - P_{b1}|\Psi_{b1}\rangle\langle\Psi_{b1}| - P_{b2}|\Psi_{b2}\rangle\langle\Psi_{b2}|$:

$$\begin{bmatrix} A\cos^2\theta_1 + B\cos^2\theta_2 & C\sin\theta_1\cos\theta_1 + D\sin\theta_2\cos\theta_2 \\ C\sin\theta_1\cos\theta_1 + D\sin\theta_2\cos\theta_2 & A\sin^2\theta_1 + B\sin^2\theta_2 \end{bmatrix}.$$

Here $A = P_{a1} - P_{b1}$, $B = P_{a2} - P_{b2}$, $C = P_{a1} + P_{b1}$, $D = P_{a2} + P_{b2}$. The expression can be translated to:

$$\frac{1}{2} \begin{bmatrix} A\cos 2\theta_1 + B\cos 2\theta_2 + A + B & C\sin 2\theta_1 + D\sin 2\theta_2 \\ C\sin 2\theta_1 + D\sin 2\theta_2 & -A\cos 2\theta_1 - B\cos 2\theta_2 + A + B \end{bmatrix}.$$

The eigenvalues can be calculated as:

$$\begin{aligned} \lambda_{\pm} &= \frac{1}{2} * (A + B \pm \sqrt{(A\cos 2\theta_1 + B\cos 2\theta_2)^2 + (C\sin 2\theta_1 + D\sin 2\theta_2)^2}) \\ &= \frac{1}{2} * (A + B \pm \sqrt{A^2\cos^2 2\theta_1 + B^2\cos^2 2\theta_2 + 2ABE + C^2\sin^2 2\theta_1 + D^2\sin^2 2\theta_2 + 2CDF}) \\ &= \frac{1}{2} * (A + B \pm \sqrt{(A^2 - C^2)\cos^2 2\theta_1 + (B^2 - D^2)\cos^2 2\theta_2 + 2ABE + (C + D)^2 + 2CDF - 2CD}) \end{aligned}$$

where we denote $\cos 2\theta_1 \cos 2\theta_2 = E$, $\sin 2\theta_1 \sin 2\theta_2 = F$. We take $A = P_{a1} - P_{b1}$, $B = P_{a2} - P_{b2}$, $C = P_{a1} + P_{b1}$, $D = P_{a2} + P_{b2}$ and $P_{a1} + P_{a2} + P_{b1} + P_{b2} = 1$ back to the expression above. Using the relation: $2AB \cos 2\theta_1 \cos 2\theta_2 + 2CD \sin 2\theta_1 \sin 2\theta_2 = AB(\cos(2\theta_1 + 2\theta_2) + \cos(2\theta_1 - 2\theta_2)) + CD(\cos(2\theta_1 - 2\theta_1) - \cos(2\theta_1 + 2\theta_2)) = 2((P_{a1}P_{a2} + P_{b1}P_{b2})\cos(2\theta_1 - 2\theta_2) - (P_{a2}P_{b1} + P_{a1}P_{b2})\cos(2\theta_1 + 2\theta_2))$, we have:

$$\lambda_{\pm} = \frac{1}{2} * (A + B \pm \{1 - 4P_{a1}P_{b1}\cos^2 2\theta_1 - 4P_{a2}P_{b2}\cos^2 2\theta_2 + 2((P_{a1}P_{a2} + P_{b1}P_{b2})\cos(2\theta_1 - 2\theta_2) - (P_{a2}P_{b1} + P_{a1}P_{b2})\cos(2\theta_1 + 2\theta_2)) - 2CD\}^{1/2}).$$

It is clear that the equation in the radical expression must be larger than 0. We have $P_{error} = \frac{1}{2}(1 - \{1 - 4P_{a1}P_{b1}|\langle \Psi_{a1} | \Psi_{b1} \rangle|^2 - 4P_{a2}P_{b2}|\langle \Psi_{a2} | \Psi_{b2} \rangle|^2 + 2(P_{a1}P_{a2} + P_{b1}P_{b2})(2|\langle \Psi_{a1} | \Psi_{a2} \rangle|^2 - 1) - 2(P_{a2}P_{b1} + P_{a1}P_{b2})(2|\langle \Psi_{a1} | \Psi_{b2} \rangle|^2 - 1) - 2CD\}^{1/2})$.

For a simple example, let $P_{a1} = P_{a2} = P_{b1} = P_{b2} = \frac{1}{4}$, and we can obtain P_{error} as:

$$P_{error} = \frac{1}{2}(1 - \frac{1}{2}\sqrt{2 - |\langle \Psi_{a1} | \Psi_{b1} \rangle|^2 - |\langle \Psi_{a2} | \Psi_{b2} \rangle|^2 + 2|\langle \Psi_{a1} | \Psi_{a2} \rangle|^2 - 2|\langle \Psi_{a1} | \Psi_{b2} \rangle|^2}).$$

The simplified P_{error} is the limited bound for our experiments. The optimal measurement is a projective measurement onto the states $\{|\Phi_a\rangle = \frac{1}{\sqrt{2}}(|0\rangle + |1\rangle), |\Phi_b\rangle = \frac{1}{\sqrt{2}}(|0\rangle - |1\rangle)\}$.

S3. COMPLETE EXPERIMENTAL DATA

Process tomography. Here we plot all the other process matrices in Fig.S2-S8, with ideal theoretical values overlaid. Data in the main text are not shown here. For clarity, we use red to represent positive and blue to represent negative. Our fidelity is computed by $\text{tr} \sqrt{\sqrt{\chi_{exp}} \chi \sqrt{\chi_{exp}}}$. Here χ_{exp} is the experimental process matrix and χ is the theoretical process matrix. The average fidelity of our gates is 0.9532.

Compression. The results of encoding different initial states into path or polarization qubit are shown in Fig.S9-S10. Data in the main text are not shown here. The blue dashed line is the bound of min-error discrimination between two different groups of nonorthogonal states.

Discrimination. The results of discriminating different initial groups of states are shown in Fig.S11-S12. The blue dashed line is the bound of min-error discrimination between two different groups of nonorthogonal states. Data in the main text are not shown here.

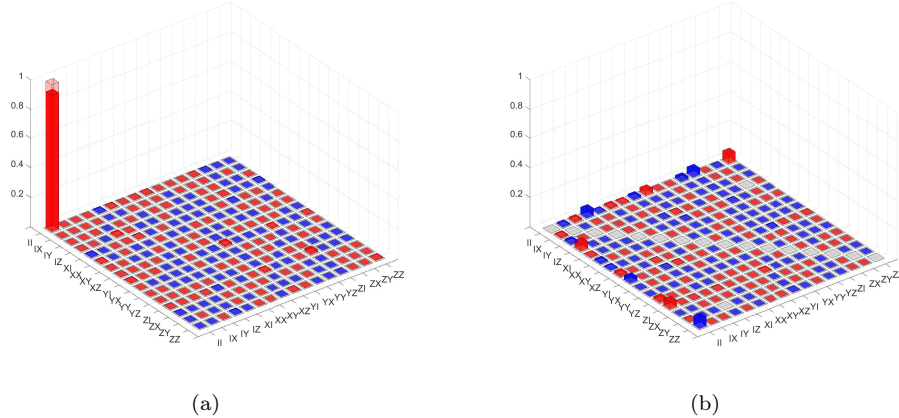


FIG. S2: Identity gate. (a) the real elements. (b) the imaginary elements. The fidelity is 0.9637.

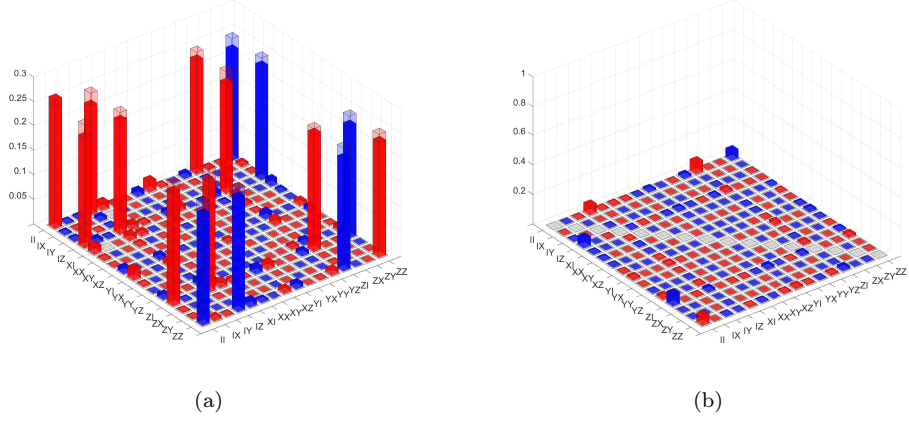


FIG. S3: Controlled-Z gate. (a) the real elements. (b) the imaginary elements. The fidelity is 0.9612.

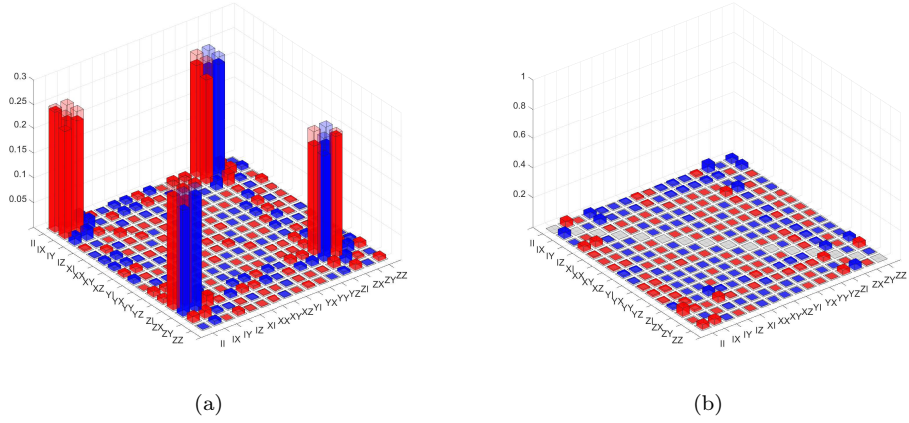


FIG. S4: Controlled NOT gate (path control polarization). (a) the real elements. (b) the imaginary elements. The fidelity is 0.9463.

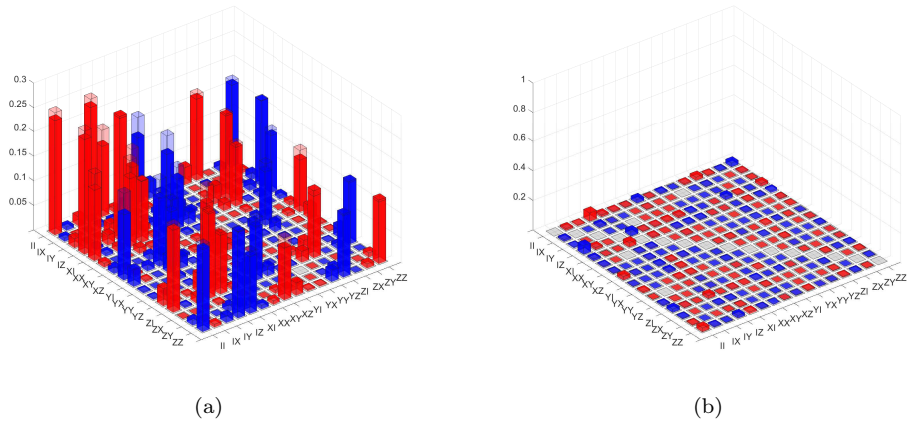


FIG. S5: Controlled Hadamard gate (polarization control path). (a) the real elements. (b) the imaginary elements. The fidelity is 0.9587.

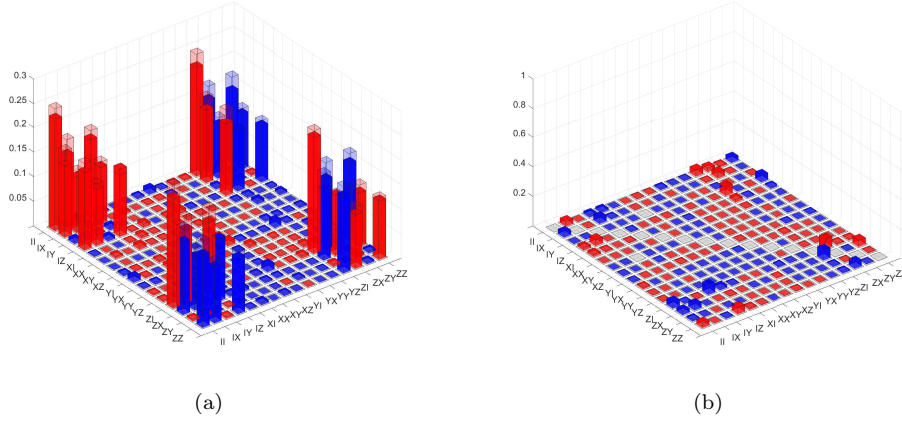


FIG. S6: Controlled Hadamard gate (path control polarization). (a) the real elements. (b) the imaginary elements. The fidelity is 0.9467.

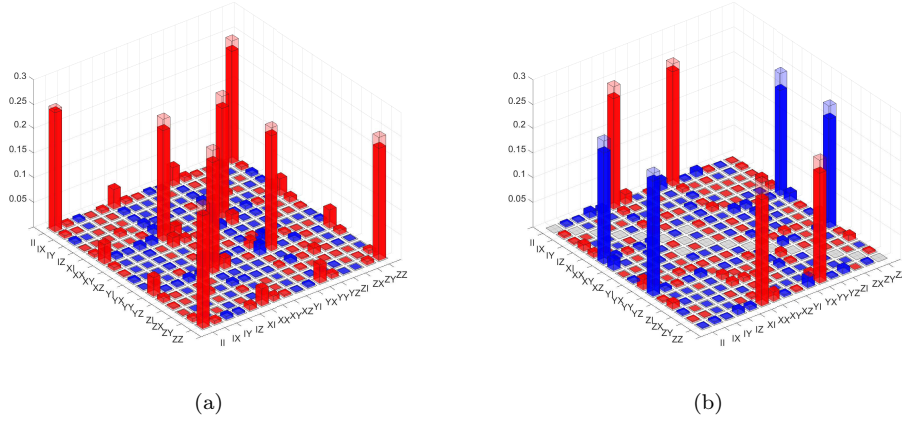


FIG. S7: iSWAP gate. (a) the real elements. (b) the imaginary elements. The fidelity is 0.9538.

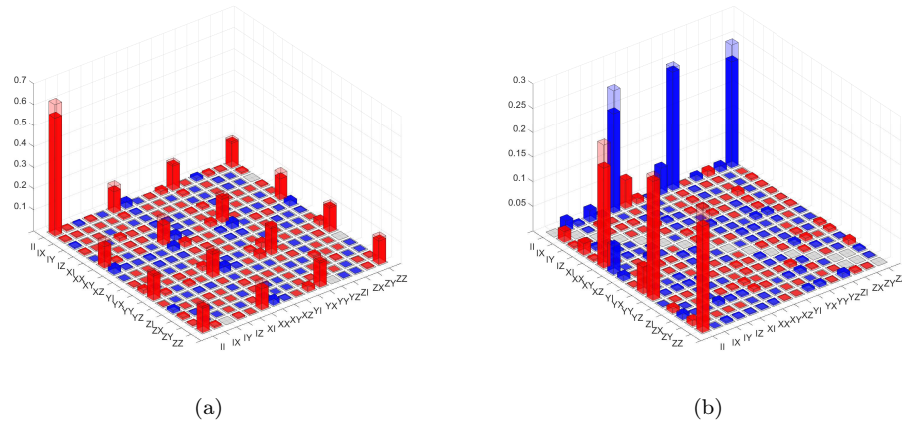


FIG. S8: \sqrt{SWAP} gate. (a) the real elements. (b) the imaginary elements. The fidelity is 0.9430.

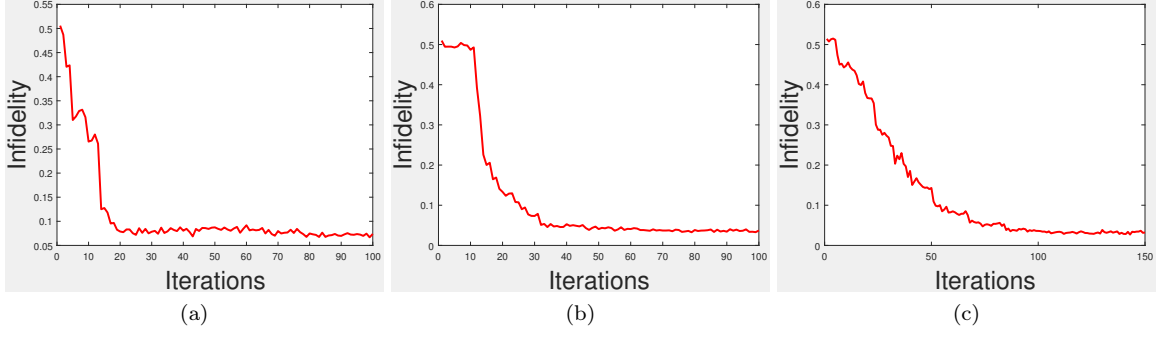


FIG. S9: The results of encoding different initial states into path qubit. (a) encode $\{\frac{1}{\sqrt{2}}|RH\rangle + \frac{1}{\sqrt{2}}|LV\rangle, \frac{1}{\sqrt{2}}|RV\rangle + \frac{1}{\sqrt{2}}|LH\rangle\}$ into path qubit. (b) encode $\{\frac{1}{\sqrt{2}}|RH\rangle + \frac{1}{\sqrt{2}}|RV\rangle, \frac{1}{\sqrt{2}}|LH\rangle + \frac{1}{\sqrt{2}}|LV\rangle\}$ into path qubit. (c) encode $\{\frac{1}{4}|RH\rangle - \frac{i}{4}|RV\rangle - \frac{1}{4}|LH\rangle + \frac{i}{4}|LV\rangle, \frac{1}{4}|RH\rangle + \frac{i}{4}|RV\rangle + \frac{1}{4}|LH\rangle + \frac{i}{4}|LV\rangle\}$ into path qubit.

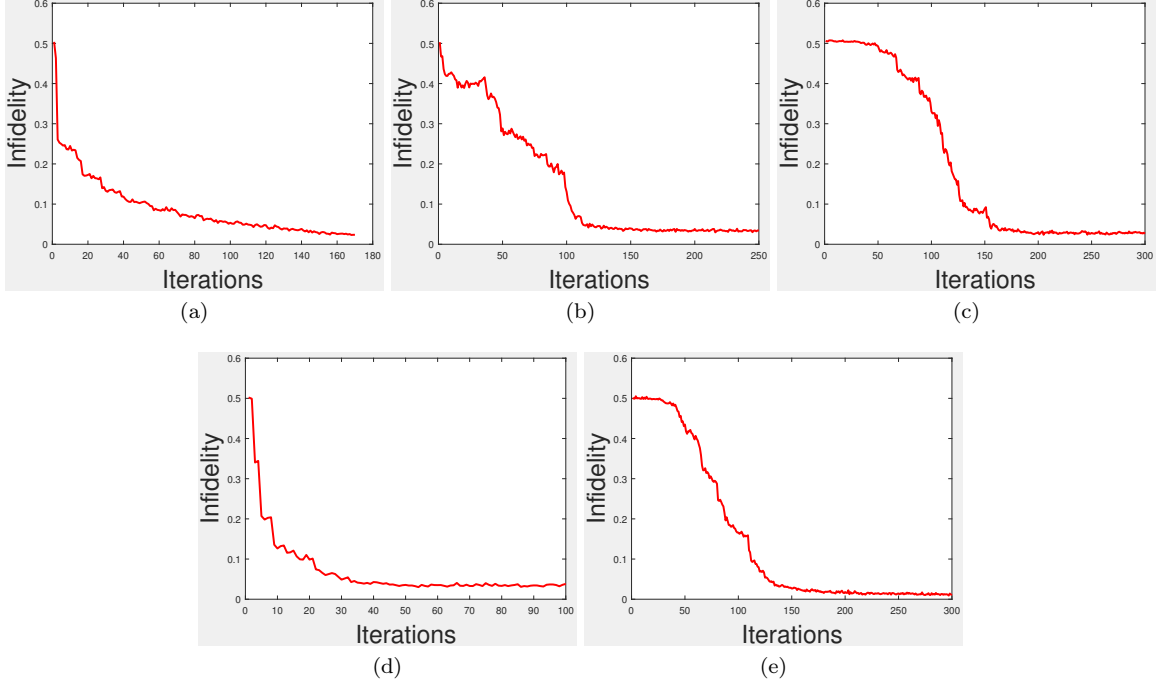


FIG. S10: The results of encoding different initial states into polarization qubit. (a) encode $\{\frac{1}{\sqrt{2}}|RH\rangle + \frac{i}{\sqrt{2}}|RV\rangle, \frac{1}{\sqrt{2}}|LH\rangle + \frac{i}{\sqrt{2}}|LV\rangle\}$ into polarization qubit. (b) encode $\{\frac{1}{\sqrt{2}}|RH\rangle + \frac{i}{\sqrt{2}}|LV\rangle, \frac{1}{\sqrt{2}}|RV\rangle + \frac{i}{\sqrt{2}}|LH\rangle\}$ into polarization qubit. (c) encode $\{\frac{1}{\sqrt{2}}|RH\rangle + \frac{1}{\sqrt{2}}|LH\rangle, \frac{1}{\sqrt{2}}|RV\rangle + \frac{1}{\sqrt{2}}|LV\rangle\}$ into polarization qubit. (d) encode $\{\frac{1}{4}|RH\rangle - \frac{i}{4}|RV\rangle - \frac{1}{4}|LH\rangle + \frac{i}{4}|LV\rangle, \frac{1}{4}|RH\rangle + \frac{i}{4}|RV\rangle + \frac{1}{4}|LH\rangle + \frac{i}{4}|LV\rangle\}$ into polarization qubit. (e) encode $\{\frac{1}{4}|RH\rangle - \frac{i}{4}|RV\rangle + \frac{1}{4}|LH\rangle + \frac{i}{4}|LV\rangle, \frac{1}{4}|RH\rangle + \frac{i}{4}|RV\rangle + \frac{1}{4}|LH\rangle + \frac{i}{4}|LV\rangle\}$ into polarization qubit.

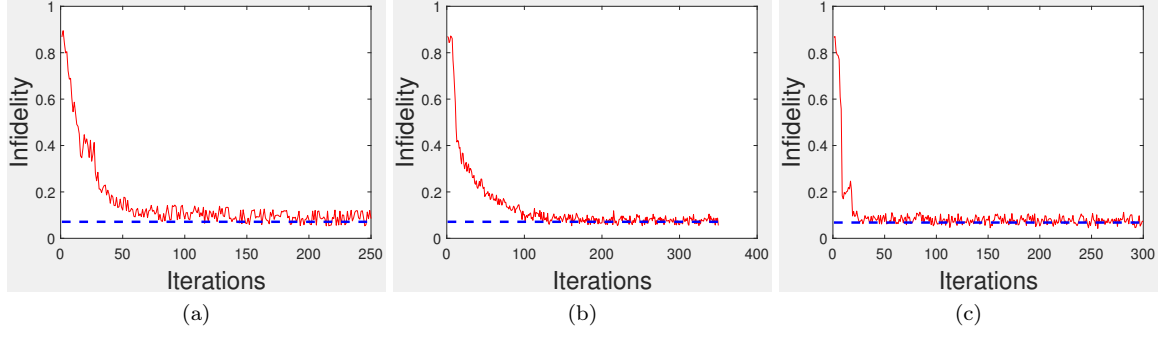


FIG. S11: The results of discriminating different initial groups of states. Here we encode different group into different path qubits. (a) encode $\{\cos \theta_{1/2}|RH\rangle + \sin \theta_{1/2}|LV\rangle, \theta_{1/2} = \pm 4^\circ\}$ & $\{\cos \theta_{3/4}|RH\rangle + \sin \theta_{3/4}|LV\rangle, \theta_{3/4} = 60^\circ \pm 4^\circ\}$ into different path qubits. (b) encode $\{\cos \theta_1|RH\rangle + \sin \theta_1|LV\rangle, \theta_1 \in [-4^\circ, 4^\circ]\}$ & $\{\cos \theta_2|RH\rangle + \sin \theta_2|LV\rangle, \theta_2 \in [56^\circ, 64^\circ]\}$ into different path qubits. (c) encode $\{\cos \theta_1|RH\rangle + \sin \theta_1|RV\rangle, \theta_1 \in [-2^\circ, 2^\circ]\}$ & $\{\cos \theta_2|RH\rangle + \sin \theta_2|RV\rangle, \theta_2 \in [58^\circ, 62^\circ]\}$ into different path qubits.

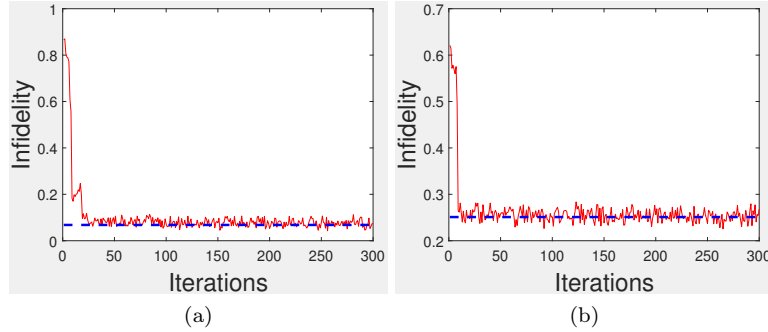


FIG. S12: The results of discriminating different initial groups of states. Here we encode different group into different polarization qubits. (a) encode $\{\cos \theta_1|RH\rangle + \sin \theta_1|RV\rangle, \theta_1 \in [-2^\circ, 2^\circ]\}$ & $\{\cos \theta_2|RH\rangle + \sin \theta_2|RV\rangle, \theta_2 \in [58^\circ, 62^\circ]\}$ into different polarization qubits. (b) encode $\{\cos \theta_1|RH\rangle + \sin \theta_1|RV\rangle, \theta_1 \in [-2^\circ, 2^\circ]\}$ & $\{\cos \theta_2|RH\rangle + \sin \theta_2|RV\rangle, \theta_2 \in [28^\circ, 32^\circ]\}$ into different polarization qubits.